

# Spin-twisted Optical Lattices: Tunable Flat Bands and Larkin-Ovchinnikov Superfluids

Xi-Wang Luo<sup>\*</sup> and Chuanwei Zhang<sup>†</sup>

*Department of Physics, The University of Texas at Dallas, Richardson, Texas 75080-3021, USA*

Moiré superlattices in twisted bilayer graphene and transition-metal dichalcogenides have emerged as a powerful tool for engineering novel band structures and quantum phases of two-dimensional quantum materials. Here we investigate Moiré physics emerging from twisting two independent hexagonal optical lattices of atomic (pseudo-)spin states (instead of bilayers), which exhibits remarkably different physics from twisted bilayer graphene. We employ a momentum-space tight-binding calculation that includes all range real-space tunnelings, and show that all twist angles  $\theta \lesssim 6^\circ$  can become magic that support gapped flat bands. Due to greatly enhanced density of states near the flat bands, the system can be driven to superfluid by weak attractive interaction. Strikingly, the superfluid phase corresponds to a Larkin-Ovchinnikov state with finite momentum pairing, resulting from the interplay between flat bands and inter-spin interactions in the unique single-layer spin-twisted lattice. Our work may pave the way for exploring novel quantum phases and twistronics in cold atomic systems.

**Introduction.**—Twisting two weakly-coupled adjacent crystal layers has been employed as a powerful tool for tailoring electronic properties of two-dimensional quantum materials [1–7], such as the formation of Moiré superlattices and flat bands. This has been evidenced by the recent groundbreaking discovery of superconductivity and correlated insulator phases in twisted bilayer graphene (TBG) [8, 9], which provide a rich platform for exploring strongly-correlated many-body phases [10–15], with the underlying physical mechanisms still under investigation [16–26]. In TBG, the interactions, the inter- and intra-layer couplings are generally fixed with very limited tunability [27–30], and magic flat bands occur only in a narrow range of very small twist angles around  $\sim 1.1^\circ$ . Going beyond layer degree of freedom in TBG, two questions naturally arise. Can lattices of other pseudo degrees be twisted to realize novel Moiré lattices and flat bands with great tunability? If so, can new physics emerge in such twisted systems?

Ultracold atoms in optical lattices provide a promising platform for exploring many-body physics in clean environments with versatile tunability [31–47]. While it is challenging to realize twisted bilayer lattices, the atomic internal states offer a pseudospin degree, where optical lattice for each spin state can be controlled independently (in particular for alkaline-earth atoms) [48–51], allowing the realization of spin-twisted-lattices and related Moiré physics. Such spin-twisted-lattices have several remarkable difference from TBG. For instance, two spins reside on one layer spatially (instead of bilayer in TBG) with their coupling provided by additional lasers, resulting in different inter-spin (compared with inter-layer in TBG) hopping and other physical parameters. The interaction is dominated by the inter-spin  $s$ -wave scattering between fermion atoms in relatively twisted spin lattices, in contrast to the uniform intra-layer interaction without spin twist in TBG. These differences can significantly affect the resulting band structures and many-

body quantum states. It is unclear whether extremely flat and gapped bands (i.e., magic-angle behaviors) can exist in spin-twisted single-layer lattice. If yes, how large can the magic angle be tuned to? Can new phases emerge from twisted inter-spin interactions?

In this Letter, we address these important questions by investigating the Moiré physics for cold atoms in two spin-dependent hexagonal lattices twisted by a relative angle, with two spin states coupled by additional uniform lasers. Our main results are:

*i)* We employ a momentum-space tight-binding method to include all range real-space tunnelings with high accuracy, which is crucial for obtaining the correct flat band structures and low-energy physics.

*ii)* Because of the tunability of inter-spin coupling strength and lattice depth, all twist angles with  $\theta \lesssim 6^\circ$  can become magic and support extremely flat and gapped bands. In general, a smaller magic angle requires weaker inter-spin coupling or a shallower lattice. When  $\theta$  is too large, no flat bands exist in the whole parameter space due to strong inter-valley coupling.

*iii)* The system can be driven to the superfluid phase by very weak attractive interactions at magic angles where the flat bands greatly enhance the density of states (DOS). Strikingly, the superfluid phase corresponds to a Larkin-Ovchinnikov (LO) state [52] with nonzero pairing momentum and staggered real-space pairing order at the hexagonal lattice scale, which does not exist in TBG and results from the interplay between flat bands and the unique inter-spin interactions of atoms in relatively twisted spin lattices.

**Model.**—To obtain independent optical lattices that can be twisted, we consider two long-lived  $^1S_0$  and  $^3P_0$  orbital states (denoted as pseudospin states  $|\uparrow\rangle$  and  $|\downarrow\rangle$ ) of alkaline-earth(-like) atoms [48–51] as shown in Fig. 1a. Atoms in state  $|\uparrow(\downarrow)\rangle$  are trapped solely by  $\lambda_{\uparrow(\downarrow)}$ -wavelength lasers, which are tuned-out for atoms in state  $|\downarrow(\uparrow)\rangle$  (e.g.,  $\lambda_{\uparrow,\downarrow} = 627\text{nm}, 689\text{nm}$  for Sr atoms).

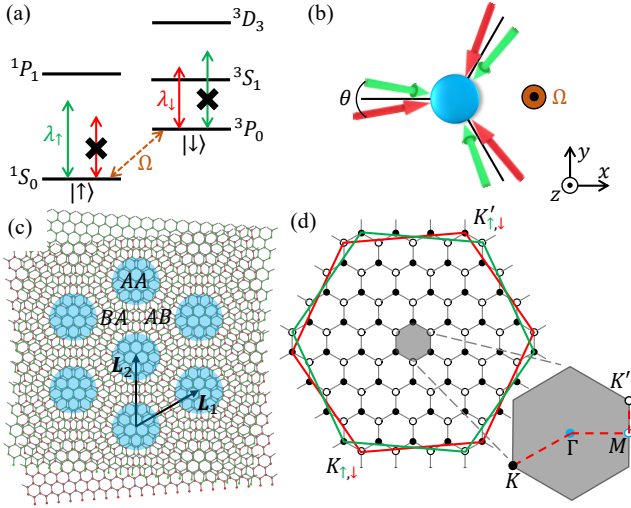


FIG. 1: (a) Energy level diagram of alkaline-earth(-like) atoms, showing how state-dependent optical lattices can be realized. (b) Laser configuration to generate spin-twisted hexagonal lattices. (c) Moiré pattern and (d) Brillouin zone of spin twisted hexagonal lattices with  $\theta = 9.43^\circ$  ( $m = 3, n = 4$ ). AA spots form a triangle lattice with AB or BA spots at the triangles' centers.  $\mathbf{L}_i$  are the primitive lattice vectors. The large hexagons in (d) correspond to the bare BZs for states  $\uparrow$  (green) and  $\downarrow$  (red), respectively.

A hexagonal lattice  $V(\mathbf{r}) = -V_0 |\sum_{j=1}^3 \epsilon_j \exp[i\mathbf{k}_{L,j} \cdot (\mathbf{r} - \mathbf{r}_0)]|^2$  is generated by intersecting three lasers at  $120^\circ$  in the  $x$ - $y$  plane with each beam linearly in-plane polarized [37]. Here  $V_0$  is the trap depth,  $\mathbf{r}_0$  is the hexagonal plaquette center,  $\mathbf{k}_{L,j}$  and  $\epsilon_j$  are the laser wave vector and polarization. Hereafter, we set momentum and energy units as  $k_R = 2\pi/\lambda_\downarrow$  and  $E_R = \hbar^2 k_R^2/2m$ . The two spin-dependent potentials  $V_{\uparrow,\downarrow}(\mathbf{r})$  are obtained through twisting  $V(\mathbf{r})$  by  $\pm\theta/2$  (see Fig. 1b). The shorter-wavelength  $\lambda_\uparrow$  lasers have an out-of-plane angle to ensure the same lattice constant for two potentials. The  $z$ -direction is tightly confined by an additional state-independent potential using the so-called magic-wavelength lasers [35], which reduces the dynamics to two dimensions (2D). The two pseudospin states are coupled by a clock laser [35] propagating along  $z$ , with  $\Omega$  the Rabi frequency.

We first consider commensurate twists with  $\cos(\theta) = \frac{n^2+m^2+4mn}{2(n^2+m^2+mn)}$  parameterized by two integers ( $m, n$ ) [1]. In Figs. 1c and 1d, the real-space pattern and Moiré Brillouin zone (BZ) are shown together with the bare BZs of two spins. For typical lattice depth, long-range tunnelings beyond nearest neighbors (especially for the inter-spin couplings where the site separations take various values and are nearly continuously distributed for small twists) should be taken into account to obtain the correct magic flat bands [53]. Small deviations in the tunneling coefficients may result in significant change in the flat band structures due to the narrow bandwidth. Here we

adopt the momentum-space Bloch basis  $\{\phi_{sl\mathbf{k}_s}(\mathbf{r})\}$  (with  $\mathbf{k}_s$  the Bloch momentum,  $l$  the band index and  $s = \uparrow, \downarrow$ ) of  $V_s(\mathbf{r})$  which spans the same tight-binding Hilbert space as the Wannier basis. When the two spins are decoupled, the lowest two bands of each spin state form two Dirac points for  $\mathbf{k}_s$  at valley  $K_s$  and  $K'_s$  in the bare BZs [53].

By projecting onto the basis  $\{\phi_{sl\mathbf{k}_s}(\mathbf{r})\}$ , the inter-spin coupling Hamiltonian reads [53]

$$H_{\uparrow\downarrow}(\mathbf{q}) = \sum_{l,l',\mathbf{g}_{\uparrow,\downarrow}} J_{\mathbf{g}_{\uparrow,\downarrow}}^{ll'}(\mathbf{q}) \alpha_{\uparrow l\mathbf{q}+\mathbf{g}_{\uparrow}}^\dagger \alpha_{\downarrow l'\mathbf{q}+\mathbf{g}_{\downarrow}} + h.c., \quad (1)$$

where  $\alpha_{sl\mathbf{k}_s}^\dagger$  are the creation operators of the Bloch states,  $\mathbf{q}$  is the superlattice Bloch momentum in the Moiré BZ and  $\mathbf{g}_s$  are the reciprocal lattice vectors of the Moiré superlattice whose summation runs over the bare BZ of state  $s$ . The inter-spin coupling coefficients are  $J_{\mathbf{g}_{\uparrow,\downarrow}}^{ll'} = \langle \phi_{\uparrow l\mathbf{q}+\mathbf{g}_{\uparrow}} | \Omega | \phi_{\downarrow l'\mathbf{q}+\mathbf{g}_{\downarrow}} \rangle$ , which already incorporate all range real-space tunnelings. Another advantage of this momentum-space approach is that if only the low-energy physics is of interest, then we only need to keep  $l$  and  $\mathbf{g}_s$  that correspond to the low-energy Bloch states [1–4], leading to a rather rapid convergence of the basis set.

Although spin-twisted optical lattices share some similarities with TBG, several important differences need be noted: 1) The two twisted optical potentials are spin-dependent and do not affect each other, while in TBG electrons in one layer can feel the potential of the other layer; 2) The inter-spin couplings in the single layer (realized by additional lasers) are different from the inter-layer tunnelings in TBG [1, 53]; 3) The optical lattice potential takes a simple cosine form, therefore the bare bands and inter-spin couplings can be obtained accurately from the Bloch states, while TBG Hamiltonians are usually based on real-space tight-binding approximation expressed in Slater-Koster parameters [1, 54–57]; 4) Long-range tunnelings are more significant due to shallow lattices considered here, which not only improve the atomic lifetime, but also increase the bare Dirac velocity. 5) Interactions are dominated by the  $s$ -wave scattering between fermion atoms in relatively twisted lattices, while electronic interactions in TBG, including both Coulomb repulsive and phonon-mediated attractive interactions, mainly involve electrons in the same layer with no relative twist [16–21]; 6) Finally, the cold-atom parameters (e.g., inter-spin tunnelings, lattice depth, lattice constant, interactions, etc.) are highly tunable, comparing with one tunable parameter, twist angle, in TBG.

**Flat bands.**—We solve the Moiré bands numerically and find that all small twist angles ( $\theta \lesssim 6^\circ$ ) can become magic that support flat bands with proper choice of inter-spin coupling strength or lattice depth. In Figs. 2a and 2b, we plot the band structures for different inter-spin coupling strengths  $\Omega$  with  $V_0 = 6$  and  $\theta = 5.086^\circ$  ( $m = 6, n = 7$ ). Similar to the TBG, the system has four low-energy bands, two of which form a Dirac cone at

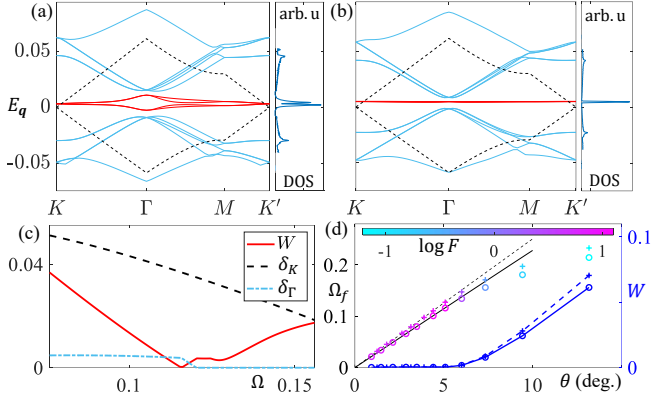


FIG. 2: (a) and (b) Moiré bands along high-symmetry lines (the red dashed lines in Fig. 1d) and DOS for  $\Omega = 0.1$  and  $\Omega = 0.116$ , respectively. We set the bare Dirac cone energy as zero. The black dashed lines are bare Dirac bands folded back to Moiré BZ. (c) Flat band width  $W$  and gaps  $\delta_{K,\Gamma}$  with other higher bands at  $K$  and  $\Gamma$  points. In (a)-(c),  $\theta = 5.086^\circ$  and  $V_0 = 6$ . (d) Critical coupling  $\Omega_f$  as a function of  $\theta$  with  $V_0 = 6$  (circles) and  $V_0 = 4$  (plus signs). Color bars show the flatness at  $\Omega = \Omega_f$  with flat band width shown by the thick blue markers and lines. The thin solid (dashed) line corresponds to  $c = 1.932$  at  $V_0 = 6$  ( $c = 1.827$  at  $V_0 = 4$ ).

the Moiré  $K$  ( $K'$ ) point where the remaining two bands are split by a tiny gap due to the inter-valley ( $K_s$ - $K'_s$ ) coupling. The Dirac cones shift to a higher energy compared to the bare ones, which is due to the couplings with states away from the valleys that have weak nonlinearity in the dispersion. The inter-spin coupling reduces the Dirac velocity significantly and enhance the DOS near the Dirac cones, as shown in Fig. 2a. The peaks in the DOS correspond to the Van Hove singularities near the Moiré  $M$  points [21, 58]. The bandwidth  $W$  of the low-energy bands and Dirac velocity are reduced further as  $\Omega$  increases and may even vanish (i.e., the twist angle becomes magic) at certain inter-spin coupling strength. We are interested in the flat bands associated with magic angles and will focus on the physics around the critical coupling  $\Omega_f$  where the narrowest bandwidth occurs (as shown in Fig. 2b). For  $\Omega \lesssim \Omega_f$ , the four low-energy bands are always separated by an energy gap from other bands in the spectrum, the gap is minimized near the Moiré  $\Gamma$  point and would close eventually as we increase  $\Omega$  above  $\Omega_f$ . Shown in Fig. 2c are the bandwidth  $W$  and gaps  $\delta_{\Gamma,K}$  (with other higher bands) versus  $\Omega$ .

In Fig. 2d, we plot  $\Omega_f$  and the corresponding bandwidth  $W$  and flatness  $F \equiv \delta_{\Gamma}/W$  as functions of the twist angle  $\theta$ . For small twists, the low-energy bands are mainly determined by the states with  $\mathbf{g}_s$  around the Dirac valleys, and have a narrow width and high flatness at  $\Omega = \Omega_f$ . In addition, the inter-valley coupling is weak, thus two conduction or valence bands (one from each valley) are nearly degenerate along the high-symmetric  $\Gamma$ - $K$  ( $K'$ ) lines [21]. We find  $\Omega_f$  almost linearly increases

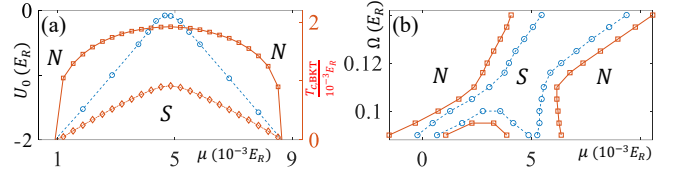


FIG. 3: (a) Phase diagrams in the  $U_0$ - $\mu$  plane at zero temperature (blue dots). The critical temperatures  $T_c$  (red squares) and  $T_{\text{BKT}}$  (red diamonds) as functions of  $\mu$  at  $U_0 = -2$ , with  $\Omega = \Omega_f$ . (b) Zero-temperature phase diagrams in the  $\Omega$ - $\mu$  plane for  $U_0 = -0.5$  (blue dots) and  $U_0 = -1$  (red squares). N and S represent the normal and superfluid phases, respectively. Common parameters:  $\theta = 5.086^\circ$ ,  $V_0 = 6$ .

with  $\theta$ . Specifically, the magic flat bands occur near  $c = \text{const.}$ , where  $c \equiv \frac{\Omega}{v_D k_D}$  is a dimensionless parameter with  $k_D = 2k_R \sin(\theta/2)$  the  $K$ - $K'$  distance in Moiré BZ and  $v_D$  the bare Dirac velocity. This is consistent with the continuum model in the TBG where  $c$  is the single parameter [3, 4]. When the twist angles are large  $\theta > 6^\circ$ , the width and splitting of the four low-energy bands become comparable or larger than the gap with other bands, and no magic flat bands exist for any  $\Omega$  since the inter-valley couplings and the effects of states away from the bare Dirac valleys become significant. For incommensurate twist angles, we can generalize the continuum model and only keep  $\mathbf{g}_s$  around one valley, which should be valid for small  $\theta$  [53]. We thus conclude that all small angles  $\theta \lesssim 6^\circ$  can support magic flat bands.

For different lattice depths  $V_0$ , the magic behaviors discussed above are similar (see Fig. 2d). Meanwhile, a smaller  $V_0$  leads to a larger  $v_D$  and thereby a stronger  $\Omega_f$  (for fixed  $\theta$ ). Long-range tunnelings are also more significant in a shallower lattice, which would effectively enhance the inter-spin couplings, leading to a slightly smaller  $c$  where the flat bands occur. The flatness may also be improved by decreasing  $V_0$  properly, since a larger  $v_D$  leads to a larger gap  $\delta_{\Gamma}$  [3, 4] and long-range tunnelings in real space can reduce inter-valley couplings that have large momentum separations. However, in the very shallow region where the dispersion-linearity around the bare Dirac cone becomes poor, the flatness starts to decrease with  $V_0$ .

**Superfluid orders.**—The narrowly dispersing flat bands suppress the kinetic energy and atom-atom interactions can lead to strongly correlated many-body ground states. Different from TBG [16–21], here the interaction of fermion atoms is dominated by  $s$ -wave scattering between atoms in relatively twisted lattices, with strength tunable through Feshbach resonance [46, 47],

$$H_{\text{int}} = U_0 \int d^2\mathbf{r} \hat{\Psi}_\uparrow^\dagger(\mathbf{r}) \hat{\Psi}_\downarrow^\dagger(\mathbf{r}) \hat{\Psi}_\downarrow(\mathbf{r}) \hat{\Psi}_\uparrow(\mathbf{r}). \quad (2)$$

We are interested in the superfluid order driven by attractive interactions. We adopt the mean-field approach [16–



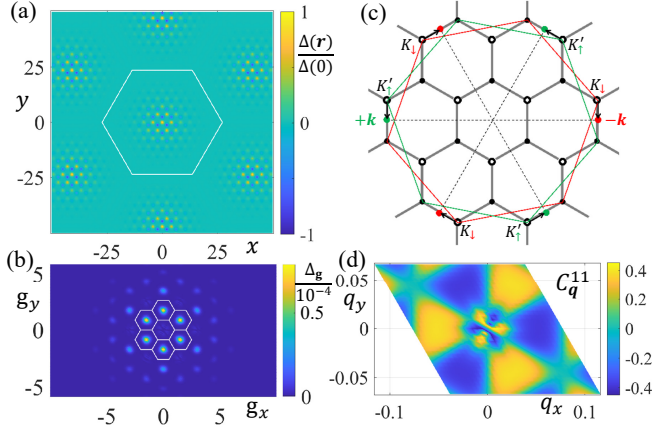


FIG. 4: (a) and (b) The superfluid pairing amplitudes in real  $[\Delta(\mathbf{r})]$  and momentum space ( $\Delta_{\mathbf{g}}$ ), respectively. The white hexagons correspond to the Moiré unit cell in (a) and the untwisted bare BZs in (b). (c) Schematic illustration of the pairing (indicated by dashed lines) in the BZs. (d) The correlation  $C_{\mathbf{q}}^{11}$ . Common parameters:  $\theta = 5.086^\circ$ ,  $V_0 = 6$ ,  $\Omega = \Omega_f$  and  $U_0 = -0.5$ .

[18] with local pairing amplitude  $\Delta(\mathbf{r}) = U_0 \langle \hat{\Psi}_\downarrow(\mathbf{r}) \hat{\Psi}_\uparrow(\mathbf{r}) \rangle$ , and assume that it has Moiré periodicity [18], which can therefore be expanded in the form  $\Delta(\mathbf{r}) = \sum_{\mathbf{g}} \Delta_{\mathbf{g}} e^{i\mathbf{g} \cdot \mathbf{r}}$  with  $\mathbf{g}$  the Moiré reciprocal lattice vectors. We use the Bogoliubov-de Gennes Hamiltonian to obtain  $\Delta(\mathbf{r})$  self-consistently [53], and retain only the four flat bands that have much larger DOS than nearby bands. We have verified that the physics is hardly affected by numerically including more nearby bands [53].

The phase diagrams for  $\theta = 5.086^\circ$ ,  $V_0 = 6$  and  $\Omega = \Omega_f$  are shown in Fig. 3a. Due to the greatly enhanced DOS near the magic flat bands at  $\Omega_f$ , the system could be driven to superfluid by very weak attractive interaction  $|U_0| \lesssim 0.08$  (at zero temperature) when the chemical potential matches the flat band energy. As  $\mu$  is tuned away from flat bands, the required interaction strength for superfluid phase increases (almost linearly). For a moderate interaction strength, the mean-field critical temperature  $T_c$  could be relatively high (reaches its largest value at  $\mu \simeq 0.005$ ) and shows a similar behavior as that predicted in TBG system [18].

Note that at finite temperature, the relevant physics in 2D is the Berezinskii-Kosterlitz-Thouless (BKT) transition [59–62] because no long-range superfluid order exists due to phase fluctuations, and the mean-field  $T_c$  is often overestimated. The BKT critical temperature  $T_{\text{BKT}}$  could be obtained from the mean-field superfluid weight [53, 63, 64], which is numerically calculated with the results shown in Fig. 3a (roughly,  $T_{\text{BKT}} \simeq 0.4T_c$ ).

In Fig. 3b, we plot the phase diagrams in the  $\Omega$ - $\mu$  plane. Away from  $\Omega_f$ , the bandwidth will be broadened, and the superfluid area becomes wider. However, it requires a lower critical temperature or stronger interaction

due to the reduced DOS. At the  $\Omega < \Omega_f$  side, the flat band DOS peak splits into two peaks (corresponding to the Van Hove singularities near the Moiré  $M$  points), therefore the superfluid phase also splits into two regions where  $\mu$  matches the DOS peaks. At the  $\Omega > \Omega_f$  side, the DOS peak is simply broadened. As the  $|U_0|$  decreases, the superfluid phase shrinks to the area around  $\Omega \simeq \Omega_f$  and  $\mu \simeq 0.005$ .

Strikingly, we find that the superfluid phase corresponds to a LO state [52], which is very different from that in TBG. The Cooper pairs have nonzero center-of-mass momentum with  $\Delta_{\mathbf{g}}$  mainly distributed around the first reciprocal lattice vector shell of the untwisted hexagonal lattice and nearly vanishing around zero momentum, leading to the staggered real-space pairing orders at the hexagonal lattice scale (Figs. 4a and 4b). The attractive  $s$ -wave interaction pairs atoms from opposite valleys, and the superfluid order is peaked in the  $AA$  regions, where the local DOS for the flat bands is strongly concentrated [53] and the wavefunction overlap between two spin states is significant. Therefore, the intra-sublattice pairing is dominant. Because atoms at the same sublattices and opposite valleys share opposite angular momenta under the threefold rotation, the pairing order has the same phase factor for the same sublattice.

Moreover, the pairing is between Moiré states at  $\pm \mathbf{q}$ , which are mainly determined by the bare Bloch states  $\phi_{sl\pm\mathbf{k}}$  at  $\pm \mathbf{k}$  nearest to the valleys (thereby contributing most to the flatbands). In Fig. 4c, the pairing between  $\uparrow$  states (green dots at  $+\mathbf{k}$ ) around valley  $K'_\uparrow$  and  $\downarrow$  states (red dots at  $-\mathbf{k}$ ) around valley  $K_\downarrow$  is illustrated schematically. Due to the relative twist,  $\pm \mathbf{k}$  are at the same side of  $K'_\uparrow$  and  $K_\downarrow$ , respectively (see the black arrows in Fig. 4c). Therefore, we have  $\phi_{\uparrow\mathbf{k}} \propto [1, e^{i\gamma_{\uparrow\mathbf{k}}}]^T$  and  $\phi_{\downarrow(-\mathbf{k})} \propto [1, e^{i\gamma_{\downarrow(-\mathbf{k})}}]^T$  on the  $A$  and  $B$  sublattice basis, with  $\gamma_{\uparrow\mathbf{k}} \simeq -\gamma_{\downarrow(-\mathbf{k})} + \pi$ . The relative phases  $\gamma_{s\mathbf{k}}$  are related to the chirality of the valleys (i.e., the Berry phase on loops surrounding the valley), which are responsible for the staggered pairing order  $\Delta(\mathbf{r}) \propto \langle \phi_{\uparrow\mathbf{k}} \phi_{\downarrow(-\mathbf{k})} \rangle \propto [1, -1]^T$  [53]. Such LO order is unique for spin-twisted system with pairing between atoms from relatively twisted lattices. In TBG, the pairing between spin-up and -down electrons in the same layer (with no relative twist) leads to ordinary BCS order [17, 18].

The correlation  $C_{\mathbf{q}}^{jj} = \langle \beta_{j'-\mathbf{q}} \beta_{j\mathbf{q}} \rangle$  shows  $f$ -wave structure ( $\beta_{j\mathbf{q}}$  is the annihilation operator for the  $j$ -th flat-band), their combined effects lead to the nearly uniform superfluid gap [53] and the pairing is  $s$ -wave. The valence bands from different valleys become degenerate along the high symmetric  $\Gamma$ - $K$  lines with avoided crossing (a tiny gap) due to inter-valley couplings, therefore  $C_{\mathbf{q}}^{11}$  changes from characterizing  $K_s$ - $K'_s$  to  $K'_s$ - $K_s$  correlations across the  $\Gamma$ - $K$  lines where its sign flips (see Fig. 4d).

**Discussion and conclusion.**—The ‘magic-angle’ physics in the spin-twisted optical lattice is very robust, supporting magic flat bands and novel LO superfluid

order in a wide range of parameter space ( $\theta$ ,  $V_0$ ,  $\Omega$ ,  $U_0$ , etc). For  $\theta \simeq 5^\circ$  and  $V_0 = 6$ , the gap between flat bands and other bands is  $\sim 10^{-2}E_R$  (about tens of Hz for Sr atoms) and can be improved further using shallower lattices (larger  $v_D$ ) or larger twists. The flat bands and enhanced DOS can be observed within atomic gas lifetime (a few seconds for the shallow lattice considered here) using spectroscopic measurements (e.g., radio-frequency spectroscopy) [65–68]. The critical superfluid temperature  $T_{c,\text{BKT}}$  is in the nanokelvin region ( $\sim 10^{-3}E_R$ ) which might be possible with the recently developing cold-atom cooling techniques [33, 69–71]. Thanks to the large twist angle  $\theta \lesssim 6^\circ$ , the Moiré unit-cell may contain less than 100 hexagons; therefore, the magic phenomena can be observed using a small system with tens of hexagons along each direction. The magic-angle physics is similar for different stackings or twist axes [53].

In summary, we study the Moiré flat band physics and the associated superfluid order in spin-twisted optical lattices for ultracold atoms, which showcase magic-angle behaviors for continuum of twists up to  $6^\circ$  and novel LO superfluid phase remarkably different from that in TBG. In future, it would be interesting to study spin-twisted lattices of other types (square, triangle, etc) or with different lattice depth and gapped bands (similar as transition metal dichalcogenide based Moiré systems [72, 73]). Moreover, one could study possible interesting many-body states under repulsive interaction and may even consider the nuclear spin states of alkaline-earth atoms with both nuclear-spin-exchange and inter-spin interactions. In all, our work provides a highly tunable playground for exploring quantum many-body physics and twistronics with novel twisted pseudo degrees of freedom.

**Acknowledgements:** We thank J. H. Pixley for helpful discussions. This work is supported by AFOSR (FA9550-16-1-0387, FA9550-20-1-0220), NSF (PHY-1806227), and ARO (W911NF-17-1-0128).

---

\* xiwang.luo@utdallas.edu

† chuanwei.zhang@utdallas.edu

- [1] J. M. B. Lopes dos Santos, N. M. R. Peres, and A. H. Castro Neto, Graphene Bilayer with a Twist: Electronic Structure, *Phys. Rev. Lett.* **99**, 256802 (2007).
- [2] S. Shallcross, S. Sharma, E. Kandelaki, and O. A. Pankratov, Electronic structure of turbostratic graphene, *Phys. Rev. B* **81**, 165105 (2010).
- [3] R. Bistritzer, A. H. MacDonald, Moiré bands in twisted double-layer graphene, *Proc. Natl. Acad. Sci. U.S.A.* **108**, 12233 (2011).
- [4] J. M. B. Lopes dos Santos, N. M. R. Peres, and A. H. Castro Neto, Continuum model of the twisted graphene bilayer, *Phys. Rev. B* **86**, 155449 (2012).
- [5] G. T. de Laissardière, D. Mayou, and L. Magaud, Localization of Dirac Electrons in Rotated Graphene Bilayers, *Nano Lett.* **10**, 804 (2010).
- [6] Y. Cao, J. Y. Luo, V. Fatemi, S. Fang, J. D. Sanchez-Yamagishi, K. Watanabe, T. Taniguchi, E. Kaxiras, and P. Jarillo-Herrero, Superlattice-Induced Insulating States and Valley-Protected Orbits in Twisted Bilayer Graphene, *Phys. Rev. Lett.* **117**, 116804 (2016).
- [7] F. Hu, S. R. Das, Y. Luan, T.-F. Chung, Y. P. Chen, and Z. Fei, Real-Space Imaging of the Tailored Plasmons in Twisted Bilayer Graphene, *Phys. Rev. Lett.* **119**, 247402 (2017).
- [8] Y. Cao, V. Fatemi, S. Fang, K. Watanabe, T. Taniguchi, E. Kaxiras, P. Jarillo-Herrero, Unconventional superconductivity in magic-angle graphene superlattices, *Nature (London)* **556**, 80 (2018).
- [9] Y. Cao, V. Fatemi, A. Demir, S. Fang, S. L. Tomarken, J. Y. Luo, J. D. Sanchez-Yamagishi, K. Watanabe, T. Taniguchi, E. Kaxiras, R. C. Ashoori, P. Jarillo-Herrero, Correlated insulator behaviour at half-filling in magic-angle graphene superlattices, *Nature (London)* **556**, 80 (2018).
- [10] A. Kerelsky, L. J. McGilly, D. M. Kennes, L. Xian, M. Yankowitz, S. Chen, K. Watanabe, T. Taniguchi, J. Hone, C. Dean, A. Rubio, and A. N. Pasupathy, Maximized electron interactions at the magic angle in twisted bilayer graphene, *Nature (London)* **572**, 95 (2019).
- [11] A. L. Sharpe, E. J. Fox, A. W. Barnard, J. Finney, K. Watanabe, T. Taniguchi, M. A. Kastner, D. Goldhaber-Gordon, Emergent ferromagnetism near three-quarters filling in twisted bilayer graphene, *Science* **365**, 605 (2019).
- [12] E. Codecido, Q. Wang, R. Koester, S. Che, H. Tian, R. Lv, S. Tran, K. Watanabe, T. Taniguchi, F. Zhang, M. Bockrath, C. N. Lau, Correlated insulating and superconducting states in twisted bilayer graphene below the magic angle, *Sci. Adv.* **5**, eaaw9770 (2019).
- [13] Y. Choi, J. Kemmer, Y. Peng, A. Thomson, H. Arora, R. Polski, Y. Zhang, H. Ren, J. Alicea, G. Refael, F. von Oppen, K. Watanabe, T. Taniguchi, and S. Nadj-Perge, Electronic correlations in twisted bilayer graphene near the magic angle, *Nat. Phys.* **15**, 1174 (2019).
- [14] G. Chen, L. Jiang, S. Wu, B. Lyu, H. Li, B. L. Chittari, K. Watanabe, T. Taniguchi, Z. Shi, J. Jung, Y. Zhang, and F. Wang, Evidence of a gate-tunable Mott insulator in a trilayer graphene moiré superlattice, *Nat. Phys.* **15**, 237 (2019).
- [15] G. W. Burg, J. Zhu, T. Taniguchi, K. Watanabe, A. H. MacDonald, and E. Tutuc, Correlated Insulating States in Twisted Double Bilayer Graphene, *Phys. Rev. Lett.* **123**, 197702 (2019).
- [16] T. J. Peltonen, R. Ojaärvi, and T. T. Heikkilä, Mean-field theory for superconductivity in twisted bilayer graphene, *Phys. Rev. B* **98**, 220504 (2018).
- [17] B. Lian, Z. Wang, and B. A. Bernevig, Twisted Bilayer Graphene: A Phonon-Driven Superconductor, *Phys. Rev. Lett.* **122**, 257002 (2018).
- [18] F. Wu, A. H. MacDonald, and I. Martin, Theory of Phonon-Mediated Superconductivity in Twisted Bilayer Graphene, *Phys. Rev. Lett.* **121**, 257001 (2018).
- [19] H. Isobe, N. F. Q. Yuan, and L. Fu, Unconventional Superconductivity and Density Waves in Twisted Bilayer Graphene, *Phys. Rev. X* **8**, 041041 (2018).
- [20] C.-C. Liu, L.-D. Zhang, W.-Q. Chen, and F. Yang, Chiral Spin Density Wave and  $d + id$  Superconductivity in the Magic-Angle-Twisted Bilayer Graphene, *Phys. Rev. Lett.*

- 121**, 217001 (2018).
- [21] J. González, and T. Stauber, Kohn-Luttinger Superconductivity in Twisted Bilayer Graphene, *Phys. Rev. Lett.* **122**, 026801 (2019).
  - [22] C. Xu, and L. Balents, Topological Superconductivity in Twisted Multilayer Graphene, *Phys. Rev. Lett.* **121**, 087001 (2018).
  - [23] X. Hu, T. Hyart, D. I. Pikulin, and E. Rossi, Geometric and Conventional Contribution to the Superfluid Weight in Twisted Bilayer Graphene, *Phys. Rev. Lett.* **123**, 237002 (2019).
  - [24] D. M. Kennes, J. Lischner, and C. Karrasch, Strong correlations and  $d + id$  superconductivity in twisted bilayer graphene, *Phys. Rev. B* **98**, 241407 (2018).
  - [25] J. F. Dodaro, S. A. Kivelson, Y. Schattner, X. Q. Sun, and C. Wang, Phases of a phenomenological model of twisted bilayer graphene, *Phys. Rev. B* **98**, 075154 (2018).
  - [26] H. C. Po, L. Zou, A. Vishwanath, and T. Senthil, Origin of Mott Insulating Behavior and Superconductivity in Twisted Bilayer Graphene, *Phys. Rev. X* **8**, 031089 (2018).
  - [27] K. Kim, A. DaSilva, S. Huang, B. Fallahazad, S. Larentis, T. Taniguchi, K. Watanabe, B. J. LeRoy, A. H. MacDonald, and E. Tutuc, Tunable moiré bands and strong correlations in small-twist-angle bilayer graphene, *Proc. Natl. Acad. Sci. U.S.A.* **114**, 3364 (2017).
  - [28] S. Carr, S. Fang, P. Jarillo-Herrero, and E. Kaxiras, Pressure dependence of the magic twist angle in graphene superlattices, *Phys. Rev. B* **98**, 085144 (2018).
  - [29] M. Yankowitz, J. Jung, E. Laksono, N. Leconte, B. L. Chittari, K. Watanabe, T. Taniguchi, S. Adam, D. Graf, and C. R. Dean, Dynamic band-structure tuning of graphene moiré superlattices with pressure, *Nature (London)* **557**, 404 (2018).
  - [30] M. Yankowitz, S. Chen, H. Polshyn, Y. Zhang, K. Watanabe, T. Taniguchi, D. Graf, A. F. Young, C. R. Dean, Tuning superconductivity in twisted bilayer graphene, *Science*, **363**, 1059 (2019).
  - [31] D. Jaksch, C. Bruder, J. I. Cirac, C. W. Gardiner, and P. Zoller, Cold Bosonic Atoms in Optical Lattices, *Phys. Rev. Lett.* **81**, 3108 (1998).
  - [32] M. Lewenstein, A. Sanpera, V. Ahufinger, B. Damski, A. Sen, and U. Sen, Ultracold atomic gases in optical lattices: mimicking condensed matter physics and beyond, *Adv. Phys.* **56**, 243 (2007).
  - [33] T. Esslinger, Fermi-Hubbard physics with atoms in an optical lattice, *Annu. Rev. Condens. Matter Phys.* **1**, 129 (2010).
  - [34] I. Bloch, J. Dalibard, and S. Nascimbène, Quantum simulations with ultracold quantum gases, *Nat. Phys.* **8**, 267 (2012).
  - [35] A. D. Ludlow, M. M. Boyd, J. Ye, E. Peik, and P. O. Schmidt, Optical atomic clocks, *Rev. Mod. Phys.* **87**, 637 (2015).
  - [36] L. Tarruell, D. Greif, T. Uehlinger, G. Jotzu, and T. Esslinger, Creating, moving and merging Dirac points with a Fermi gas in a tunable honeycomb lattice, *Nature (London)* **483**, 302 (2012).
  - [37] T. Li, L. Duca, M. Reitter, F. Grusdt, E. Demler, M. Endres, M. Schleier-Smith, I. Bloch, and U. Schneider, Bloch state tomography using Wilson lines, *Science* **352**, 1094 (2016).
  - [38] T. Akatsuka, M. Takamoto, and H. Katori, Optical lattice clocks with non-interacting bosons and fermions, *Nat. Phys.* **4**, 954 (2008).
  - [39] S. L. Campbell, R. B. Hutson, G. E. Marti, A. Goban, N. Darkwah Oppong, R. L. McNally, L. Sonderhouse, J. M. Robinson, W. Zhang, B. J. Bloom, and J. Ye, A Fermi-degenerate three-dimensional optical lattice clock, *Science* **358**, 90 (2017).
  - [40] L. F. Livi, G. Cappellini, M. Diem, L. Franchi, C. Clivati, M. Frittelli, F. Levi, D. Calonico, J. Catani, M. Inguscio, and L. Fallani, Synthetic dimensions and spin-orbit coupling with an optical clock transition, *Phys. Rev. Lett.* **117**, 220401 (2016).
  - [41] S. Kolkowitz, S. L. Bromley, T. Bothwell, M. L. Wall, G. E. Marti, A. P. Koller, X. Zhang, A. M. Rey, and J. Ye, Spin-orbit-coupled fermions in an optical lattice clock, *Nature (London)* **542**, 66 (2017).
  - [42] T. Graß, R. W. Chhajlany, L. Tarruell, V. Pellegrini, and M. Lewenstein, Proximity effects in cold atom artificial graphene, *2D Materials* **4**, 015039 (2016).
  - [43] Y. Fu, E. J. Küig, J. H. Wilson, Y.-Z. Chou, and J. H. Pixley, Magic-angle semimetals, [arXiv:1809.04604](https://arxiv.org/abs/1809.04604).
  - [44] Y.-Z. Chou, Y. Fu, J. H. Wilson, E. J. König, and J. H. Pixley, Magic-angle semimetals with chiral symmetry, *Phys. Rev. B* **101**, 235121 (2020).
  - [45] T. Salamon, A. Celi, R. W. Chhajlany, I. Frérot, M. Lewenstein, L. Tarruell, and D. Rakshit, Simulating Twistronics without a Twist, *Phys. Rev. Lett.* **125**, 030504 (2020).
  - [46] C. Chin, R. Grimm, P. Julienne, and E. Tiesinga, Feshbach resonances in ultracold gases, *Rev. Mod. Phys.* **82**, 1225 (2010).
  - [47] R. Zhang, Y. Cheng, P. Zhang, and H. Zhai, Controlling the interaction of ultracold alkaline-earth atoms, *Nat. Rev. Phys.* **2**, 213 (2020).
  - [48] S. G. Porsev, A. D. Ludlow, M. M. Boyd, and J. Ye, Determination of Sr properties for a high-accuracy optical clock, *Phys. Rev. A* **78**, 032508 (2008).
  - [49] A. J. Daley, M. M. Boyd, J. Ye, and P. Zoller, Quantum Computing with Alkaline-Earth-Metal Atoms, *Phys. Rev. Lett.* **101**, 170504 (2008).
  - [50] L. Riegger, N. Darkwah Oppong, M. Höfer, D. R. Fernandes, I. Bloch, and S. Fölling, Localized Magnetic Moments with Tunable Spin Exchange in a Gas of Ultracold Fermions, *Phys. Rev. Lett.* **120**, 143601 (2018).
  - [51] A. González-Tudela, and J. I. Cirac, Cold atoms in twisted-bilayer optical potentials, *Phys. Rev. A* **100**, 053604 (2019).
  - [52] A. I. Larkin and Y. N. Ovchinnikov, Nonuniform state of superconductors, *Zh. Eksp. Teor. Fiz.* **47**, 1136 (1964) [*Sov. Phys. JETP* **20**, 762 (1965)].
  - [53] See supplementary materials for more details about Moiré tight-binding Hamiltonian, superfluid orders, the effects of different stackings or twist axes, and the differences of our system with TBG system.
  - [54] P. Moon, and M. Koshino, Energy spectrum and quantum Hall effect in twisted bilayer graphene, *Phys. Rev. B* **85**, 195458 (2012).
  - [55] T. Nakanishi, and T. Ando, Conductance of Crossed Carbon Nanotubes, *J. Phys. Soc. Jpn.* **70**, 1647 (2001).
  - [56] J. C. Slater and G. F. Koster, Simplified LCAO Method for the Periodic Potential Problem, *Phys. Rev.* **94**, 1498 (1954).
  - [57] S. Fang, and E. Kaxiras, Electronic structure theory of weakly interacting bilayers, *Phys. Rev. B* **93**, 235153

- (2016).
- [58] N. F. Q. Yuan, H. Isobe, and L. Fu, Magic of high-order van Hove singularity, *Nat. Commun.* **10**, 5769 (2019).
  - [59] V. L. Berezinskii, Destruction of long-range order in one-dimensional and two-dimensional systems having a continuous symmetry group I. Classical systems, *Sov. Phys. JETP* **32**, 493 (1971).
  - [60] J. M. Kosterlitz and D. Thouless, Long range order and metastability in two dimensional solids and superfluids.(Application of dislocation theory), *J. Phys. C* **5**, L124 (1972).
  - [61] M. Gong, G. Chen, S. Jia, and C. Zhang, Searching for Majorana Fermions in 2D Spin-Orbit Coupled Fermi Superfluids at Finite Temperature, *Phys. Rev. Lett.* **109**, 105302 (2012).
  - [62] Y. Xu and C. Zhang, Berezinskii-Kosterlitz-Thouless Phase Transition in 2D Spin-Orbit-Coupled Fulde-Ferrell Superfluids, *Phys. Rev. Lett.* **114**, 110401 (2015).
  - [63] X.-J. Liu, K. T. Law, and T. K. Ng, Realization of 2D Spin-Orbit Interaction and Exotic Topological Orders in Cold Atoms, *Phys. Rev. Lett.* **112**, 086401 (2014).
  - [64] A. Julku, L. Liang, and P. Törmä, Superfluid weight and Berezinskii-Kosterlitz-Thouless temperature of spin-imbalanced and spin-orbit-coupled Fulde-Ferrell phases in lattice systems, *New J. Phys.* **20**, 085004 (2018).
  - [65] C. Chin, M. Bartenstein, A. Altmeyer, S. Riedl, S. Jochim, J. H. Denschlag, R. Grimm, Observation of the Pairing Gap in a Strongly Interacting Fermi Gas, *Science* **305**, 1128 (2004).
  - [66] J. T. Stewart, J. P. Gaebler, and D. S. Jin, Using photoemission spectroscopy to probe a strongly interacting Fermi gas, *Nature (London)* **454**, 744 (2008).
  - [67] C. H. Schunck, Y. Shin, A. Schirotzek, and W. Ketterle, Determination of the fermion pair size in a resonantly interacting superfluid, *Nature (London)* **454**, 739 (2008).
  - [68] J. Zhang, H. Hu, X.-J. Liu, and H. Pu, Fermi gases with synthetic spin-orbit coupling, *Annu. Rev. Cold At. Mol.* **2** 81 (2014).
  - [69] D. Greif, T. Uehlinger, G. Jotzu, L. Tarruell, T. Esslinger, Short-Range Quantum Magnetism of Ultracold Fermions in an Optical Lattice, *Science* **340**, 1307 (2013).
  - [70] A. Mazurenko, C. S. Chiu, G. Ji, M. F. Parsons, M. Kanász-Nagy, R. Schmidt, F. Grusdt, E. Demler, D. Greif, and M. Greiner, A cold-atom Fermi-Hubbard antiferromagnet, *Nature (London)* **545**, 462 (2017).
  - [71] B. Yang, H. Sun, C.-J. Huang, H.-Y. Wang, Y. Deng, H.-N. Dai, Z.-S. Yuan, J.-W. Pan, Cooling and entangling ultracold atoms in optical lattices, *Science* **369**, 550 (2020).
  - [72] F. Wu, T. Lovorn, E. Tutuc, and A. H. MacDonald, Hubbard Model Physics in Transition Metal Dichalcogenide Moiré Bands, *Phys. Rev. Lett.* **121**, 026402 (2018).
  - [73] Y. Tang, L. Li, T. Li, Y. Xu, S. Liu, K. Barmak, K. Watanabe, T. Taniguchi, A. H. MacDonald, J. Shan, and K. F. Mak, Simulation of Hubbard model physics in WSe<sub>2</sub>/WS<sub>2</sub> moiré superlattices, *Nature (London)* **579**, 353 (2020).

## SUPPLEMENTARY MATERIALS

### Momentum-space tight-binding characterization

The Bloch states of the hexagonal lattice  $V(\mathbf{r}) = -V_0 |\sum_{j=1}^3 \epsilon_j \exp[i\mathbf{k}_{L,j} \cdot (\mathbf{r} - \mathbf{r}_0)]|^2$  can be written as  $\phi_{l\mathbf{k}}(\mathbf{r}) = e^{i\mathbf{k} \cdot \mathbf{r}} u_{l\mathbf{k}}(\mathbf{r})$ . The periodic part can be expanded as  $u_{l\mathbf{k}}(\mathbf{r}) = \sum_{\mathbf{p}} c_{l\mathbf{k}}^{\mathbf{p}} e^{i\mathbf{p} \cdot \mathbf{r}}$ , where  $\mathbf{p} = p_1 \mathbf{e}_1 + p_2 \mathbf{e}_2$  with  $\mathbf{e}_i$  the primitive reciprocal lattice vectors and  $p_i$  integers. By substituting expansion of  $\phi_{l\mathbf{k}}(\mathbf{r})$  into the Schrödinger equation  $[-\frac{\nabla^2}{2m} + V(\mathbf{r})]\phi_{l\mathbf{k}} = \mathcal{E}_{l\mathbf{k}}\phi_{l\mathbf{k}}$ , the Bloch states (i.e., the coefficients  $c_{l\mathbf{k}}^{\mathbf{p}}$ ) and bands can be obtained. The bare Bloch bands  $\mathcal{E}_{sl\mathbf{k}_s}$  and states  $\phi_{sl\mathbf{k}_s}$  of the two pseudospin states can be obtained similarly, as shown in Fig. S1. Here we keep the expansion coefficients up to  $p_i = \pm 6$  in the calculation. We see that the two lowest bands (i.e.,  $\mathcal{E}_{sl\mathbf{k}_s}$  with  $l = 1, 2$ ), which have a gap from higher bands, form two Dirac cones at valleys  $K_s$  and  $K'_s$  [1]. For typical lattice depths, the two Dirac bands are asymmetric with respect to Dirac-point energy  $E = 0$  due to the long-range tunnelings beyond nearest neighbors that break the sublattice symmetry. Such effect is more significant for shallower lattices.

We are interested in the low-energy physics near the Dirac points, therefore we only retain the two-lowest bare Dirac bands (i.e.,  $\mathcal{E}_{sl\mathbf{k}_s}$  with  $l = 1, 2$ ) and drop all higher bands with  $l > 2$  safely. That is, we keep only one Wannier orbital at each hexagonal lattice site, and these Wannier orbitals form the full tight-binding basis set. We find that it is more convenient to work in the Bloch basis  $\{\phi_{sl\mathbf{k}_s}\}$ , which is equivalent to the Wannier basis up to a Fourier transformation. For commensurate twists  $\cos(\theta) = \frac{n^2+m^2+4mn}{2(n^2+m^2+mn)}$ , one can fold the bare Brillouin zone of each spin states to the Moiré Brillouin zone. The inter-spin coupling coefficient can be obtained as  $\langle \phi_{\uparrow l\mathbf{k}_{\uparrow}} | \Omega | \phi_{\downarrow l'\mathbf{k}_{\downarrow}} \rangle = \delta_{\mathbf{q}, \mathbf{q}'} J_{\mathbf{g}_{\uparrow}\mathbf{g}_{\downarrow}}^{ll'}(\mathbf{q})$ , where  $\mathbf{k}_{\uparrow} = \mathbf{q} + \mathbf{g}_{\uparrow}$  and  $\mathbf{k}_{\downarrow} = \mathbf{q}' + \mathbf{g}_{\downarrow}$ , with  $\mathbf{g}_s$  the Moiré reciprocal lattice vectors and  $\mathbf{q}$  the Moiré Bloch momentum that is a good quantum number. We obtain the Hamiltonian Eq. (1) in the main text, which incorporates all range real-space tunnelings with high accuracy. Another advantage of this momentum-space approach is that we only need to keep  $\mathbf{g}_s$  around the Dirac cones to correctly characterize the low-energy physics at small twist angles, leading to rather rapid convergence of the basis set.



Now we show how to evaluate the inter-spin coupling coefficients

$$\begin{aligned}
\langle \phi_{\uparrow l \mathbf{k}_{\uparrow}} | \Omega | \phi_{\downarrow l' \mathbf{k}_{\downarrow}} \rangle &= \Omega \int d^2 \mathbf{r} e^{-i \mathbf{k}_{\uparrow} \cdot \mathbf{r}} u_{\uparrow l \mathbf{k}_{\uparrow}}^*(\mathbf{r}) e^{i \mathbf{k}_{\downarrow} \cdot \mathbf{r}} u_{\downarrow l' \mathbf{k}_{\downarrow}}(\mathbf{r}) \\
&= \Omega \sum_{\mathbf{M}} e^{i(\mathbf{q}' - \mathbf{q}) \cdot \mathbf{M}} \langle u_{\uparrow l \mathbf{k}_{\uparrow}} | e^{i(\mathbf{k}_{\downarrow} - \mathbf{k}_{\uparrow}) \cdot (\mathbf{r} - \mathbf{M})} | u_{\downarrow l' \mathbf{k}_{\downarrow}} \rangle_{\mathbf{M}} \\
&= \Omega \delta_{\mathbf{q}, \mathbf{q}'} \langle u_{\uparrow l \mathbf{k}_{\uparrow}} | e^{i(\mathbf{g}_{\downarrow} - \mathbf{g}_{\uparrow}) \cdot \mathbf{r}} | u_{\downarrow l' \mathbf{k}_{\downarrow}} \rangle.
\end{aligned} \tag{S1}$$

Here  $\mathbf{M}$  denotes the Moiré lattice vectors, and the term  $\langle \cdots \rangle_{\mathbf{M}}$  in the second line (with integral over the  $\mathbf{M}$ -th Moiré unit cell) is independent of  $\mathbf{M}$ . The coefficients  $J_{\mathbf{g}_{\uparrow} \mathbf{g}_{\downarrow}}^{ll'}(\mathbf{q})$  is

$$\begin{aligned}
J_{\mathbf{g}_{\uparrow} \mathbf{g}_{\downarrow}}^{ll'}(\mathbf{q}) &= \Omega \langle u_{\uparrow l \mathbf{k}_{\uparrow}} | e^{i(\mathbf{g}_{\downarrow} - \mathbf{g}_{\uparrow}) \cdot \mathbf{r}} | u_{\downarrow l' \mathbf{k}_{\downarrow}} \rangle \\
&= \Omega \sum_{\mathbf{p}_{\uparrow}, \mathbf{p}_{\downarrow}} c_{\uparrow l \mathbf{k}_{\uparrow}}^{\mathbf{p}_{\uparrow}*} c_{\downarrow l' \mathbf{k}_{\downarrow}}^{\mathbf{p}_{\downarrow}} \int d^2 \mathbf{r} e^{i(\mathbf{p}_{\downarrow} - \mathbf{p}_{\uparrow} + \mathbf{g}_{\downarrow} - \mathbf{g}_{\uparrow}) \cdot \mathbf{r}} \\
&= \Omega \sum_{\mathbf{p}_{\uparrow}, \mathbf{p}_{\downarrow}, \mathbf{M}} c_{\uparrow l \mathbf{k}_{\uparrow}}^{\mathbf{p}_{\uparrow}*} c_{\downarrow l' \mathbf{k}_{\downarrow}}^{\mathbf{p}_{\downarrow}} \frac{e^{i(\mathbf{p}_{\downarrow} - \mathbf{p}_{\uparrow} + \mathbf{g}_{\downarrow} - \mathbf{g}_{\uparrow}) \cdot \mathbf{L}_1} - 1}{(\mathbf{p}_{\downarrow} - \mathbf{p}_{\uparrow} + \mathbf{g}_{\downarrow} - \mathbf{g}_{\uparrow}) \cdot \mathbf{L}_1} \frac{1 - e^{i(\mathbf{p}_{\downarrow} - \mathbf{p}_{\uparrow} + \mathbf{g}_{\downarrow} - \mathbf{g}_{\uparrow}) \cdot \mathbf{L}_2}}{(\mathbf{p}_{\downarrow} - \mathbf{p}_{\uparrow} + \mathbf{g}_{\downarrow} - \mathbf{g}_{\uparrow}) \cdot \mathbf{L}_2} \\
&= \Omega \sum_{\mathbf{p}_{\uparrow}, \mathbf{p}_{\downarrow}, \mathbf{M}} c_{\uparrow l \mathbf{k}_{\uparrow}}^{\mathbf{p}_{\uparrow}*} c_{\downarrow l' \mathbf{k}_{\downarrow}}^{\mathbf{p}_{\downarrow}} \delta_{\mathbf{p}_{\downarrow} - \mathbf{p}_{\uparrow}, \mathbf{g}_{\uparrow} - \mathbf{g}_{\downarrow}}.
\end{aligned} \tag{S2}$$

To obtain the last step, we have used  $\mathbf{p}_s \cdot \mathbf{L}_1 = 2\pi(m p_{s1} + n p_{s2})$  (similarly for  $\mathbf{L}_2$ ), since  $\mathbf{p}_s = p_{s1} \mathbf{e}_{s\mathbf{k}_1} + p_{s2} \mathbf{e}_{s\mathbf{k}_2}$  and  $\mathbf{L}_1 = m \mathbf{e}_{s1} + n \mathbf{e}_{s2}$ , with  $\mathbf{e}_{s1}, \mathbf{e}_{s2}$  ( $\mathbf{e}_{s\mathbf{k}_1}, \mathbf{e}_{s\mathbf{k}_2}$ ) the primitive (reciprocal) lattice vectors of trap  $V_s$ .

With these coupling coefficients, we can diagonalize the single particle Hamiltonian  $H_0 = H_{\uparrow} + H_{\downarrow} + H_{\uparrow\downarrow}$ . In the Moiré Bloch eigenbasis  $\{\psi_{j\mathbf{q}}\}$ , it reads

$$H_0 = \sum_{j, \mathbf{q}} E_{j\mathbf{q}} \beta_{j\mathbf{q}}^{\dagger} \beta_{j\mathbf{q}}. \tag{S3}$$

The typical distributions of  $\psi_{j\mathbf{q}}(\mathbf{r}, s)$  are shown in Figs. S2a and S2b. Atoms are mainly distributed around the AA region for all  $\mathbf{q}$  except a small area near  $\mathbf{q} = \Gamma$ , where atoms become more uniformly distributed. As a result, the interaction and thereby the pairing is weak at  $\Gamma$  point.

The above results and the Hamiltonian Eq. (1) in the main text apply for any commensurate twist angles. For incommensurate twist angles, there are no well-defined Moiré patterns and Moiré bands if the twist angle is too large. However, if the twist angle is small enough, Moiré patterns can form even for incommensurate twist. In this case, the low-energy physics is mainly determined by the states around the Dirac valleys, and the inter-valley coupling is also negligible. Therefore, we can adopt a similar approach as the continuum model by only keeping  $\mathbf{g}_s$  around one valley in the Hamiltonian, and the inter-spin couplings can be obtained using Eq. S2. In Fig. S2c, we plot the Moiré bands at a small incommensurate twist angle using the generalized one-valley continuum model mentioned above.

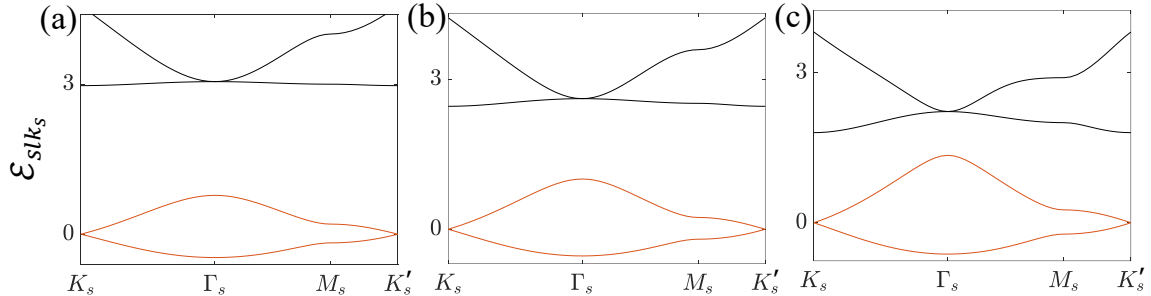


FIG. S1: Band structures of a hexagonal lattice with (a)  $V_0 = 6E_R$ , (b)  $V_0 = 4E_R$  and (c)  $V_0 = 2E_R$ . We have shifted the Dirac-point energy to  $E = 0$ . For a shallower lattice, the tunnelings (both short and long range tunnelings) are stronger, therefore, the Dirac velocity is larger and the nonlinearity of the dispersion around the Dirac points is stronger. In addition, the two Dirac bands become more asymmetric with respect to the Dirac-point energy  $E = 0$  due to the enhanced long-range tunnelings that break the sublattice symmetry.



We also plot the Moiré bands at a small commensurate twist angle using the one-valley continuum model approach and compare it with the results based on the full tight-binding basis (see Fig. S2d). Their agreement confirms the validation of the one-valley continuum model at small twist angles.

As we discussed in the main text, the energy scales of the magic physics is small and at the order of  $10^{-3}E_R$ . Therefore, in the Wannier basis, long-range (intra- and inter-spin) tunnelings beyond nearest neighbors that are  $\gtrsim 10^{-3}E_R$  should be taken into account to obtain correct magic flat bands [2–5]. In particular, the inter-spin site separations take various values and are nearly continuously distributed for small twists, therefore the on-site, NN, next-NN, etc., inter-spin tunnelings should be considered even when the tunneling cutoff distance is small. The inter-spin tunnelings are also highly anisotropic, which depend on both the relative orientation and distance between the corresponding sites due to the three-fold rotational symmetry of the Wannier orbitals. A small deviation in the tunnelling coefficients may result in significant change in the band structures near the ‘magic angle’ due to the narrow bandwidths and approximate degeneracy of the flat bands. The simplified real-space tight-binding model in [6], which assumes a simply isotropic Gaussian Wannier function and includes only the nearest-neighbor intra-spin tunneling and on-site inter-spin couplings, has significant deviation in determining the bands at small twist angles.

To elaborate more on the effects of long-range real-space tunnelings, we first solve for the maximally localized Wannier functions  $w_{s,j}(\mathbf{r})$  (with  $j$  the site index) of the two spin-dependent lattices, then calculate the band structures using the real-space tight-binding Hamiltonian

$$H_s = \sum_{j,j'} t_{jj'} \alpha_{s,j}^\dagger \alpha_{s,j'}$$

and

$$H_{\uparrow\downarrow} = \sum_{j,j'} J_{jj'} \alpha_{\uparrow,j}^\dagger \alpha_{\downarrow,j'} + h.c.,$$

where  $\alpha_{s,j}^\dagger$  is the creation operator of the Wannier orbitals, and the tunneling coefficients are  $t_{jj'} = \int d^2\mathbf{r} w_{s,j}^*(\mathbf{r}) [-\nabla_{\mathbf{r}}^2 + V_s(\mathbf{r})] w_{s,j'}(\mathbf{r})$  and  $J_{jj'} = \int d^2\mathbf{r} w_{\uparrow,j}^*(\mathbf{r}) \Omega w_{\downarrow,j'}(\mathbf{r})$ . For the lattice depth considered in this paper, we have  $(t_0; t_1; t_2; t_3; t_4; t_5) = (-4.3458; -0.1967; 0.0166; -0.0047; -0.0025; 0.0009)E_R$  for  $V_0 = 6E_R$  and  $(t_0; t_1; t_2; t_3; t_4; t_5) = (-2.2498; -0.2351; 0.0245; -0.0089; -0.0045; 0.002)E_R$  for  $V_0 = 4E_R$ , with  $t_{jj'} = t_{\tilde{i}}$  if site  $j$  is the  $\tilde{i}$ -th neighbor of site  $j'$  (where  $t_0$  is the on-site energy). Therefore, the cutoff distance for tunneling should be up to the 5-th nearest neighbors of the bare hexagonal lattice. The inter-spin coupling  $J_{jj'}$  is nearly continuously distributed which decays exponentially with site separation (the on-site tunneling rate is close to  $\Omega$ ). In Figs. S3a and S3b, we show the band structures for different cutoff distance. We see that the flat band energy is largely shifted (by  $\sim 0.25t_1$ ) for a cutoff only to the 1st nearest neighbors of the bare hexagonal lattice. Nevertheless, magic flat bands are still observed with

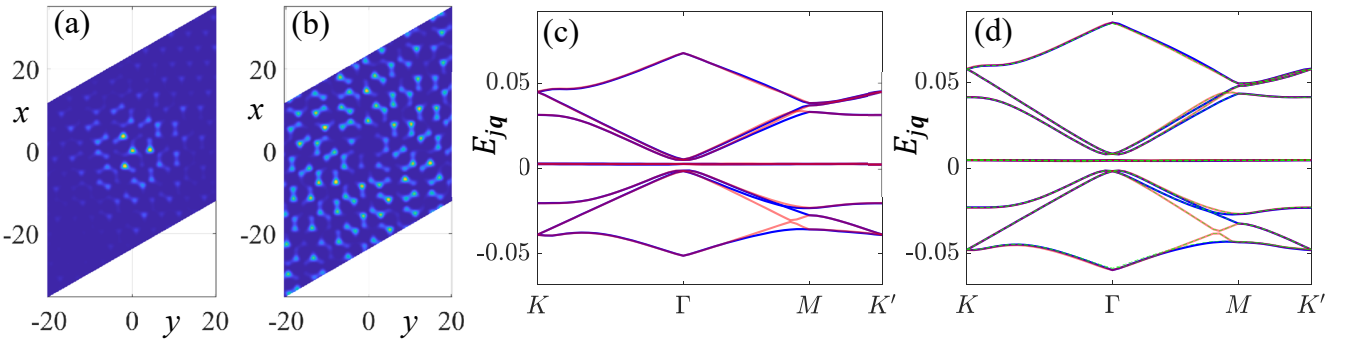


FIG. S2: (a) and (b) Typical density distributions of the Moire flat band Bloch states  $\psi_{jq}(\mathbf{r}, \downarrow)$  in one Moiré unit cell for  $\mathbf{q} = K$  and  $\mathbf{q} = \Gamma$ , respectively. Atoms are mainly distributed around the AA region for  $\mathbf{q} = K$  and become more uniformly distributed for  $\mathbf{q} = \Gamma$ . Other parameters are  $\theta = 5.086^\circ$ ,  $V_0 = 6E_R$  and  $\Omega = 0.116$ . (c) Moiré bands at incommensurate twist angle  $\theta = 4^\circ$  based on the generalized one-valley continuum model, with  $V_0 = 6E_R$  and  $\Omega = 0.0915$ . The red and blue lines are bands from  $K_s$  and  $K'_s$  valleys, respectively. We have retained a shell (containing 37 MBZs up to the third Moiré reciprocal lattice vector shell) around the valley to construct the basis set. (d) Moiré bands at commensurate twist  $\theta = 5.086^\circ$  based on the generalized one-valley continuum model, with  $V_0 = 6E_R$  and  $\Omega = 0.116$ . The green thin dashed lines are Moiré bands obtained using the full tight-binding basis.

a larger width (which can be reduced further by tuning  $\Omega$ ), indicating the robustness of the magic-angle physics.

### Superfluid orders

The mean-field interaction reads

$$\begin{aligned} H_{\text{int}} &= U_0 \int d^2\mathbf{r} \hat{\Psi}_\uparrow^\dagger(\mathbf{r}) \hat{\Psi}_\downarrow^\dagger(\mathbf{r}) \hat{\Psi}_\downarrow(\mathbf{r}) \hat{\Psi}_\uparrow(\mathbf{r}) \\ &= \int d^2\mathbf{r} [\hat{\Psi}_\uparrow^\dagger(\mathbf{r}) \hat{\Psi}_\downarrow^\dagger(\mathbf{r}) \Delta(\mathbf{r}) + \hat{\Psi}_\downarrow(\mathbf{r}) \hat{\Psi}_\uparrow(\mathbf{r}) \Delta^*(\mathbf{r}) - \frac{|\Delta(\mathbf{r})|^2}{U_0}] \end{aligned} \quad (\text{S4})$$

with local pairing amplitude  $\Delta(\mathbf{r}) = U_0 \langle \hat{\Psi}_\downarrow(\mathbf{r}) \hat{\Psi}_\uparrow(\mathbf{r}) \rangle = \sum_{\mathbf{g}} \Delta_{\mathbf{g}} e^{i\mathbf{g} \cdot \mathbf{r}}$ . We expand the field operator in the Moiré Bloch basis  $\hat{\Psi}_s(\mathbf{r}) = \sum_{j,\mathbf{q}} \beta_{j\mathbf{q}} \psi_{j\mathbf{q}}(\mathbf{r}, s)$  and obtain the gap equation

$$\Delta_{\mathbf{g}} = U_0 \sum_{j',j,\mathbf{q}} \chi_{j'j}^{\mathbf{q}}(\mathbf{g}) C_{\mathbf{q}}^{j'j} [\Delta(\mathbf{r})], \quad (\text{S5})$$

where  $\chi_{j'j}^{\mathbf{q}}(\mathbf{g}) = \frac{1}{L} \int d^2\mathbf{r} e^{-i\mathbf{g} \cdot \mathbf{r}} \psi_{j'-\mathbf{q}}(\mathbf{r}, \downarrow) \psi_{j\mathbf{q}}(\mathbf{r}, \uparrow)$ . The correlation  $C_{\mathbf{q}}^{j'j} = \langle \beta_{j'-\mathbf{q}} \beta_{j\mathbf{q}} \rangle$  can be obtained by solving the Bogoliubov-de Gennes (BdG) Hamiltonian

$$H_{\text{BdG}} = \sum_{j,\mathbf{q}} (E_{j\mathbf{q}} - \mu) \beta_{j\mathbf{q}}^\dagger \beta_{j\mathbf{q}} + \sum_{j,j',\mathbf{q}} [\bar{\Delta}_{jj'}(\mathbf{q}) \beta_{j\mathbf{q}}^\dagger \beta_{j'-\mathbf{q}}^\dagger + h.c.] \quad (\text{S6})$$

with  $\bar{\Delta}_{jj'}(\mathbf{q}) = L \sum_{\mathbf{g}} \Delta_{\mathbf{g}} \chi_{j'j}^{\mathbf{q}*}(\mathbf{g})$ . We solve the gap equation self-consistently by retaining only the four flat bands which have much larger DOS than nearby bands.

As we discussed in the main text, at finite temperature, the relevant physics is the Berezinskii-Kosterlitz-Thouless (BKT) transition since there is no long-range superfluid order in two dimensions due to phase fluctuations, and free vortex-antivortex pairs are formed spontaneously below a critical temperature  $T_{\text{BKT}}$  [7, 8]. The critical temperature  $T_c$  by mean-field theory is often overestimated. Nevertheless, the mean-field critical temperature  $T_c$  provides an upper bound of  $T_{\text{BKT}}$ . Furthermore, the true BKT transition temperature could be obtained from the mean-field superfluid weight  $\rho_s$  which can be calculated based on current response [9, 10]. On the Moiré superlattice scale, our system corresponds to an *s*-wave superfluid, we introduce a slowly varying superfluid phase  $\Delta(\mathbf{r}) \rightarrow \Delta(\mathbf{r}) e^{i\Theta(\mathbf{r},\tau)} =$

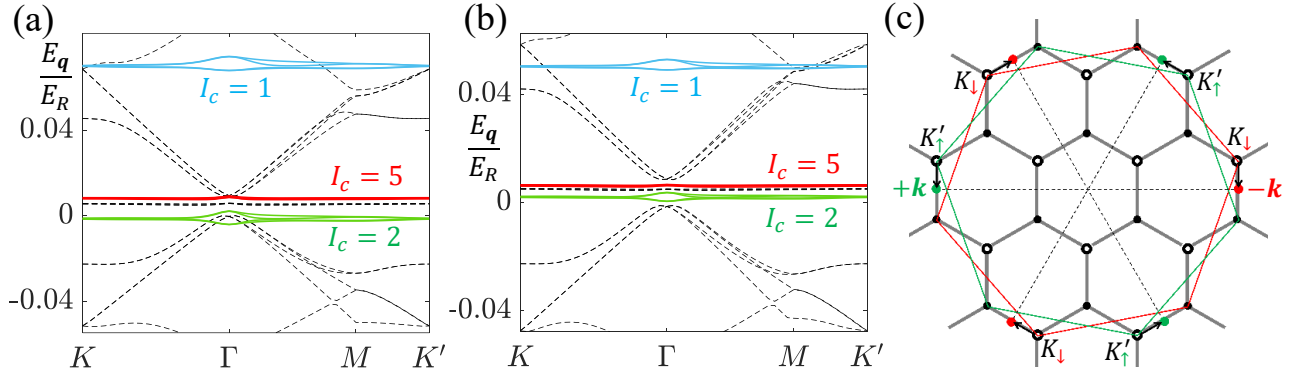


FIG. S3: (a) and (b) Moiré bands based on real-space tight-binding Hamiltonian for  $V_0 = 4E_R$  and  $V_0 = 6E_R$ , respectively. For cutoff distance  $I_c$ , we keep the (intra- and inter-spin) tunnelings with site separation not greater than the  $I_c$ -th neighbor separation of the bare hexagonal lattice (e.g., we keep  $t_{\tilde{i}}$  with  $\tilde{i} \leq I_c$ ). The blue, green and red solid lines correspond to the cutoff distance up to the 1st, 2nd and 5-th neighbors of the bare hexagonal lattice. The thin dashed lines are the results of the momentum-space tight-binding Hamiltonian. Other parameters are  $\theta = 5.086^\circ$  and  $\Omega = \Omega_f$ . (c) Schematic illustration of the pairing (indicated by dashed lines) in the Brillouin zones, between  $\uparrow$  states (green dots at  $+k$ ) around valley  $K'_\uparrow$  and  $\downarrow$  states (red dots at  $-k$ ) around valley  $K'_\downarrow$ . The two pairing states are located at the same side of the corresponding valleys (as indicated by the black arrows), and thus the relative phase between *A* and *B* sublattice sites (which is related to the chirality of the valley) leads to the staggered pairing order.

$\sum_{\mathbf{g}} \Delta_{\mathbf{g}} e^{i\mathbf{g} \cdot \mathbf{r}} e^{i\Theta(\mathbf{r}, \tau)}$ , and the phase  $\Theta(\mathbf{r}, \tau) = \mathbf{Q} \cdot \mathbf{r}$  (with  $\mathbf{Q} \rightarrow 0$ ) leads to a supercurrent  $\mathbf{j}_s = \rho_s \mathbf{Q}$ . The supercurrent can also be calculated using the variation of the free energy  $\mathbf{j}_s = \frac{1}{L} \langle \frac{\delta H_{\text{BdG}}}{\delta \mathbf{Q}} \rangle$ , the superfluid weight is obtained by  $\rho_s = \mathbf{j}_s / \mathbf{Q}$ , and the BKT transition temperature is given by  $T_{\text{BKT}} = \frac{\pi}{2} \rho_s (T_{\text{BKT}})$  [9, 10]. Here the BdG Hamiltonian reads

$$H_{\text{BdG}}(\mu, \Delta, \mathbf{Q}) = \sum_{j, \mathbf{q}} (E_{j\mathbf{q}} - \mu) \beta_{j\mathbf{q}}^\dagger \beta_{j\mathbf{q}} + \sum_{j, j', \mathbf{q}} [\bar{\Delta}_{jj'}(\mathbf{q}, \mathbf{Q}) \beta_{j\mathbf{q}+\mathbf{Q}/2}^\dagger \beta_{j'-\mathbf{q}+\mathbf{Q}/2}^\dagger + h.c.] \quad (\text{S7})$$

where  $\bar{\Delta}_{jj'}(\mathbf{q}, \mathbf{Q}) = L \sum_{\mathbf{g}} \Delta_{\mathbf{g}} \chi_{jj'}^{\mathbf{q}, \mathbf{Q}*}(\mathbf{g})$  and  $\chi_{jj'}^{\mathbf{q}, \mathbf{Q}}(\mathbf{g}) = \frac{1}{L} \int d^2 \mathbf{r} e^{-i\mathbf{g} \cdot \mathbf{r}} \psi_{j'-\mathbf{q}+\mathbf{Q}/2}(\mathbf{r}, \downarrow) \psi_{j\mathbf{q}+\mathbf{Q}/2}(\mathbf{r}, \uparrow)$ . The gap equation is  $\Delta_{\mathbf{g}} = U_0 \sum_{j', j, \mathbf{q}} \chi_{jj'}^{\mathbf{q}, \mathbf{Q}}(\mathbf{g}) C_{\mathbf{q}, \mathbf{Q}}^{j'j}$  with  $C_{\mathbf{q}, \mathbf{Q}}^{j'j} = \langle \beta_{j'-\mathbf{q}+\mathbf{Q}/2} \beta_{j\mathbf{q}+\mathbf{Q}/2} \rangle$ .

Typically,  $\rho_s(T)$  is nearly a constant at low temperature  $T$ , and therefore we use the following approximation  $T_{\text{BKT}} \simeq \frac{\pi}{2} \rho_s(T=0)$ . We numerically calculate  $T_{\text{BKT}}$  (the results are shown in Fig. 3a in the main text) and find that  $T_{\text{BKT}} \simeq 0.4T_c$ . In particular, we first set  $\Theta(\mathbf{r}, \tau) = 0$  and solve for the order parameter  $\Delta_0(\mathbf{r})$  with fixed chemical potential  $\mu$ , the corresponding zero-temperature free energy is  $\mathcal{F}(\mathbf{Q}=0) \equiv \frac{1}{L} \langle H_{\text{BdG}}(\mu, \Delta_0, \mathbf{Q}=0) \rangle$ . Then we introduce the superfluid phase  $\Theta(\mathbf{r}, \tau) = \mathbf{Q} \cdot \mathbf{r}$  by setting the order parameter as  $\Delta_0(\mathbf{r}) e^{i\mathbf{Q} \cdot \mathbf{r}}$ , and we calculate the free energy  $\mathcal{F}(\mathbf{Q}) \equiv \frac{1}{L} \langle H_{\text{BdG}}(\mu, \Delta_0, \mathbf{Q}) \rangle$ . Since  $\mathbf{j}_s = \rho_s \mathbf{Q} = \frac{\delta F(\mathbf{Q})}{\delta \mathbf{Q}}$  for  $\mathbf{Q} \rightarrow 0$  at  $T=0$ , we have  $F(\mathbf{Q}) - F(0) = \frac{1}{2} \rho_s \mathbf{Q}^2 = \frac{1}{2} \rho_s (\nabla \Theta)^2$  and the superfluid weight is calculated as  $\rho_s(T=0) = 2 \times \frac{F(\mathbf{Q}) - F(0)}{\mathbf{Q}^2}$ . The BKT critical temperature is obtained as  $T_{\text{BKT}} \simeq \pi \times \frac{F(\mathbf{Q}) - F(0)}{\mathbf{Q}^2}$ .

It can be verified that, the results based on current response are consistent with those obtained through the effective action based on quantum field theory. The partition function can be written as  $Z = \text{Tr}(e^{-H/T}) = \int \mathcal{D}[\bar{\Psi}, \Psi] e^{-S_{\text{eff}}[\bar{\Psi}, \Psi]}$ . The effective action is

$$S_{\text{eff}}[\bar{\Psi}, \Psi] = \int_0^{1/T} d\tau \left[ \int d^2 \mathbf{r} \sum_s \bar{\Psi}_s \partial_\tau \Psi_s + \mathcal{H}(\bar{\Psi}, \Psi) \right], \quad (\text{S8})$$

with  $\mathcal{H}(\bar{\Psi}, \Psi) = \int d^2 \mathbf{r} \{ \sum_s [\bar{\Psi}_s (-\nabla^2 + V_s - \mu) \Psi_s + \bar{\Psi}_s \Omega \Psi_s] + U_0 \bar{\Psi}_\uparrow \bar{\Psi}_\downarrow \Psi_\downarrow \Psi_\uparrow \}$  obtained by replacing field operator  $\hat{\Psi}_s^\dagger(\mathbf{r}, t)$  and  $\hat{\Psi}_s(\mathbf{r}, t)$  with Grassman field number  $\bar{\Psi}_s$  and  $\Psi_s$  in the Hamiltonian, and  $\tau$  is the imaginary time. We can integrate out the quartic interaction term by Hubbard-Stratonovich transformation, where the order parameter  $\Delta$  is defined. By further integrating out fermion fields, the partition function reads  $Z = \int \mathcal{D}[\Delta^*, \Delta] e^{-S_{\text{eff}}[\Delta^*, \Delta]}$  with

$$S_{\text{eff}}[\Delta^*, \Delta] = \int_0^{1/T} d\tau \int d^2 \mathbf{r} \frac{-|\Delta|^2}{U_0} - \frac{1}{2} \text{Tr} \ln(i\omega_m + M_{\text{BdG}}) + \frac{1}{T} \sum (\mathcal{E}_{sl\mathbf{k}_s} - \mu). \quad (\text{S9})$$

Where  $M_{\text{BdG}}$  is the BdG matrix in the Nambu basis, and  $\omega_m$  are Matsubara frequencies. For a static phase  $\Theta(\mathbf{r}, \tau) = \mathbf{Q} \cdot \mathbf{r}$ , the effective action induced by the phase fluctuation is

$$S_{\text{fluc}} = \frac{1}{2} \text{Tr} \ln[i\omega_m + M_{\text{BdG}}(0)] - \frac{1}{2} \text{Tr} \ln[i\omega_m + M_{\text{BdG}}(\mathbf{Q})]. \quad (\text{S10})$$

We can further sum over Matsubara frequencies and obtain

$$S_{\text{fluc}} = \frac{1}{2} \sum_{j, \mathbf{q}} \ln \cosh \frac{E_{\text{BdG}}(j, \mathbf{q}, \mathbf{0})}{2T} - \frac{1}{2} \sum_{j, \mathbf{q}} \ln \cosh \frac{E_{\text{BdG}}(j, \mathbf{q}, \mathbf{Q})}{2T}, \quad (\text{S11})$$

with  $E_{\text{BdG}}(j, \mathbf{q}, \mathbf{Q})$  the BdG eigenfrequencies, which can be calculated numerically. It is hard to proceed further to obtain an analytical expression of  $S_{\text{fluc}}(\mathbf{Q})$  due to the complicated setup. Instead, we assume  $S_{\text{fluc}}$  takes the form

$$S_{\text{fluc}} = \int_0^{1/T} d\tau \int d^2 \mathbf{r} \frac{1}{2} \rho_s (\nabla \Theta)^2 = \int_0^{1/T} d\tau \int d^2 \mathbf{r} \frac{1}{2} \rho_s \mathbf{Q}^2 \quad (\text{S12})$$

for  $\mathbf{Q} \rightarrow 0$  and a static phase  $\Theta(\mathbf{r}, \tau) = \mathbf{Q} \cdot \mathbf{r}$  [7, 8], leading to  $\rho_s = \frac{2T}{\mathbf{Q}^2 L} S_{\text{fluc}}$ . In the low temperature limit  $T \rightarrow 0$ , we have

$$\lim_{T \rightarrow 0} \frac{T}{L} S_{\text{fluc}} = \frac{1}{2L} \sum_{j, \mathbf{q}, E < 0} [E_{\text{BdG}}(j, \mathbf{q}, \mathbf{Q}) - E_{\text{BdG}}(j, \mathbf{q}, \mathbf{0})] = F(\mathbf{Q}) - F(0). \quad (\text{S13})$$

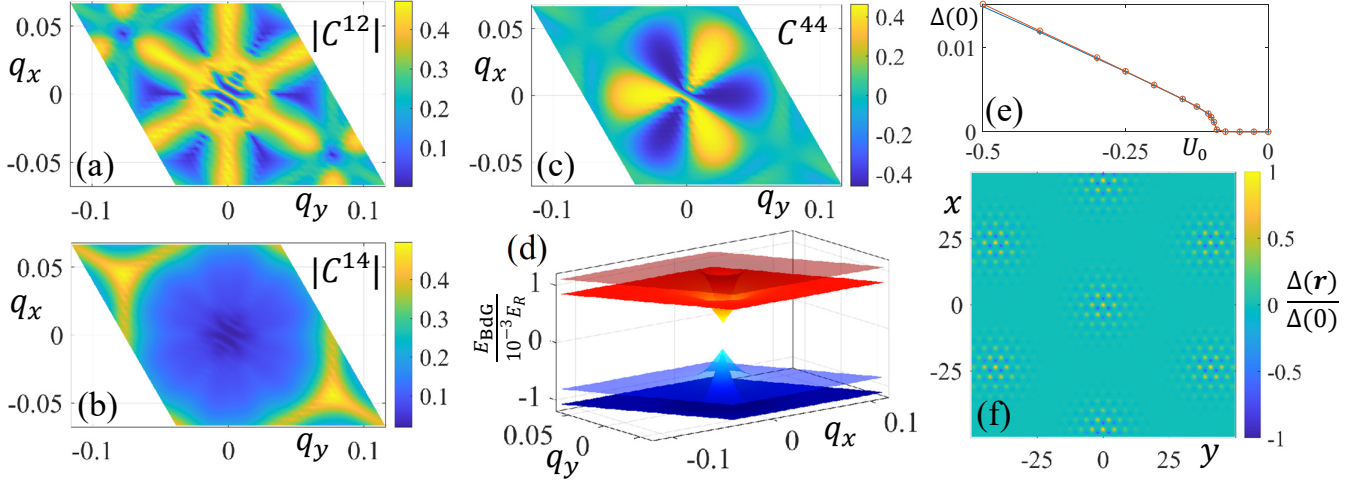


FIG. S4: (a)-(c) The correlations  $C_{\mathbf{q}}^{j'j}$  for different  $j', j$  with  $U_0 = -0.5$ . (d) The superfluid band structures (two middle particle/hole bands are not shown). (e) Superfluid order  $\Delta(\mathbf{r} = 0)$  as a function of  $U_0$  obtained by retaining 12 bands (circles) and 4 bands (plus signs) with  $\mu = 0.00485$ . (f) Superfluid order  $\Delta(\mathbf{r})$  at  $U_0 = -0.5$ . Common parameters:  $\theta = 5.086^\circ$ ,  $V_0 = 6E_R$  and  $\Omega = 0.116$ .

Therefore, the results based on current response are consistent with those obtained through the effective action. We have numerically verified that,  $\rho_s(T) = \frac{2T}{LQ^2} S_{\text{fluc}}$  is nearly a constant at low temperature with  $\rho_s(T_{\text{BKT}}) \simeq \rho_s(T = 0)$ , and  $T_{\text{BKT}} = \frac{\pi}{2} \rho_s(T_{\text{BKT}}) \simeq \frac{\pi}{2} \rho_s(T = 0)$  is a very good approximation.

The attractive  $s$ -wave interaction pairs atoms from opposite valleys of the bare hexagonal lattice and the intra-sublattice pairing is dominant. Note that the pairing is between Moiré momentum  $\pm \mathbf{q}$ , which is mainly determined by the bare Bloch states  $\phi_{\uparrow \mathbf{k}}$  and  $\phi_{\downarrow -\mathbf{k}}$  nearest to the valleys (which contribute most to the flat bands). Due to the relative twist,  $\pm \mathbf{k}$  are located at the same side of the corresponding valleys (as illustrated in Fig. S3c). Therefore, we have  $\phi_{\uparrow \mathbf{k}} \propto [1, e^{i\gamma_{\uparrow \mathbf{k}}}]^T$  and  $\phi_{\downarrow -\mathbf{k}} \propto [1, e^{i\gamma_{\downarrow -\mathbf{k}}}]^T$  in the  $A$  and  $B$  sublattice basis, with the relative phases  $\gamma_{\uparrow \mathbf{k}} \simeq -\gamma_{\downarrow -\mathbf{k}} + \pi$  (which are related to the chirality of the valleys, i.e., the Berry phase on loops surrounding the valley). The relative phase  $\gamma_{s\mathbf{k}}$  between  $A$  and  $B$  sublattice sites are responsible for the Larkin-Ovchinnikov phase with staggered pairing order  $\Delta(\mathbf{r}) \propto \langle \phi_{\uparrow \mathbf{k}} \phi_{\downarrow -\mathbf{k}} \rangle \propto [1, -1]^T$ .

The correlations  $C_{\mathbf{q}}^{j'j} = \langle \beta_{j' -\mathbf{q}} \beta_{j\mathbf{q}} \rangle$  for different  $j, j'$  are shown in Figs. S4a-c. The pairing is mainly between bands from different valleys, and the conduction bands from different valleys become degenerate along the high symmetric  $\Gamma$ - $K$  lines with avoided crossing (a tiny gap) due to inter-valley couplings. As we discussed in the main text,  $C_{\mathbf{q}}^{11}$

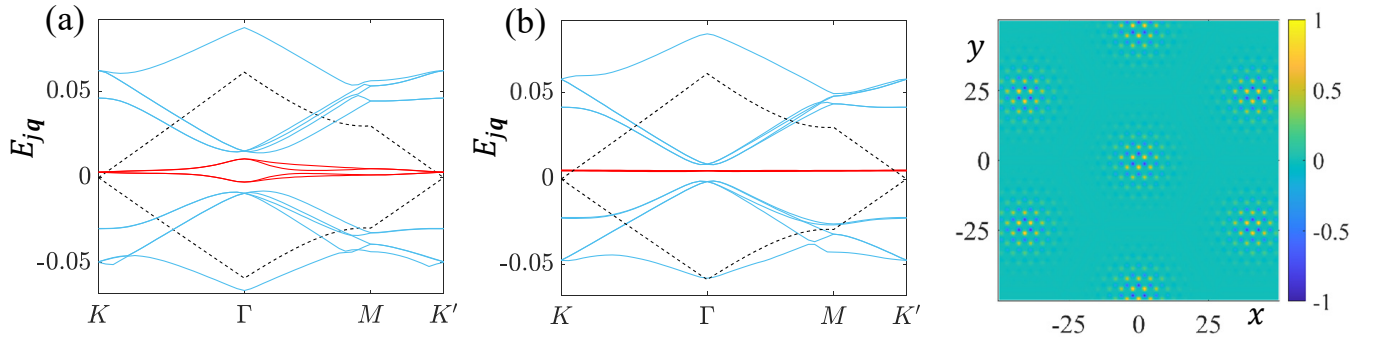


FIG. S5: (a) and (b) Moiré bands for  $AB$  stacking with twist axis at one coinciding site (where  $A$  site of  $V_{\uparrow}$  coincides with  $B$  site of  $V_{\downarrow}$ ). All other parameters in (a) and (b) are the same as Figs. 2a and 2b in the main text, respectively. The bands are almost identical with that in Figs. 2a and 2b in the main text, except that the two valence (conduction) flat bands become degenerate at  $K$  and  $K'$  points and a tiny gap develops between the valence and conduction flat bands. (c) The normalized pairing order  $\Delta(\mathbf{r})$  (maximum is normalized to 1) starting from  $AA$  stacking with twist axis at one hexagon center. Other parameters are  $\theta = 5.086^\circ$ ,  $V_0 = 6E_R$ ,  $\Omega = \Omega_f = 0.116$  and  $U_0 = -0.5$ .



changes from characterizing  $K_s$ - $K'_s$  to  $K'_s$ - $K_s$  correlations; therefore,  $C_{\mathbf{q}}^{11}$  changes the sign across the  $\Gamma$ - $K$  lines where  $C_{\mathbf{q}}^{12}$  is mainly distributed. This means that though  $C_{\mathbf{q}}^{jj}$  show  $f$ -wave structures, their combined effects lead to the nearly uniform superfluid gap (see Fig. S4d) and the pairing is  $s$ -wave. The small superfluid gap (weak pairing) at  $\Gamma$  is due to the nearly uniform Moiré wavefunction there (see Fig. S2b). Moreover, we also calculate the results by including 8 nearby Moiré bands (12 bands in total with 4 flat bands, 4 higher and 4 lower bands) for comparison, and find that these nearby bands have very little effects on the phase diagram and superfluid order (as shown in Figs. S4e and S4f).

In the above mean-field approach, we have assumed a real-space pairing order. Alternatively, we can assume the momentum-space pairing order. In particular, we first write the interaction Hamiltonian as

$$H_{\text{int}} = \sum U_{j_1 j_2; j_3 j_4}^{\mathbf{Q}; \mathbf{q}, \mathbf{q}'} \beta_{j_1 \mathbf{Q} + \mathbf{q}}^\dagger \beta_{j_2 \mathbf{Q} - \mathbf{q}}^\dagger \beta_{j_3 \mathbf{Q} - \mathbf{q}'} \beta_{j_4 \mathbf{Q} + \mathbf{q}'}$$

with  $U_{j_1 j_2; j_3 j_4}^{\mathbf{Q}; \mathbf{q}, \mathbf{q}'} = U_0 \int d^2 \mathbf{r} \psi_{j_1 \mathbf{Q} + \mathbf{q}}^*(\mathbf{r}, \uparrow) \psi_{j_2 \mathbf{Q} - \mathbf{q}}^*(\mathbf{r}, \downarrow) \psi_{j_3 \mathbf{Q} - \mathbf{q}'}(\mathbf{r}, \downarrow) \psi_{j_4 \mathbf{Q} + \mathbf{q}'}(\mathbf{r}, \uparrow)$ . Here  $\mathbf{Q}$ ,  $\mathbf{q}$  and  $\mathbf{q}'$  are superlattice momenta in the Moiré BZ. We restrict the interaction to the  $\mathbf{Q} = 0$  BCS channel, and assume the momentum-space order  $\bar{\Delta}_{j_1 j_2}(\mathbf{q}) = \sum_{j_3, j_4, \mathbf{q}'} U_{j_1 j_2; j_3 j_4}^{\mathbf{0}; \mathbf{q}, \mathbf{q}'} C_{\mathbf{q}'}^{j_3 j_4}$ . The correlation  $C_{\mathbf{q}'}^{j_3 j_4}$  can be obtained by solving the BdG Hamiltonian

$$H_{\text{BdG}} = \sum_{j, \mathbf{q}} (E_{j\mathbf{q}} - \mu) \beta_{j\mathbf{q}}^\dagger \beta_{j\mathbf{q}} + \sum_{j_1, j_2, \mathbf{q}} [\bar{\Delta}_{j_1 j_2}(\mathbf{q}) \beta_{j_1 \mathbf{q}}^\dagger \beta_{j_2 - \mathbf{q}}^\dagger + h.c.], \quad (\text{S14})$$

which allows us to obtain the superfluid order  $\bar{\Delta}_{j_1 j_2}(\mathbf{q})$  self-consistently. Using this approach, we calculate superfluid order by keeping only the four flat bands and find that the orders  $\bar{\Delta}_{j_1 j_2}(\mathbf{q})$  are the same (up to tiny numeric errors) as those obtained by assuming a real-space pairing order [i.e.,  $\sum_{j_3, j_4, \mathbf{q}'} U_{j_1 j_2; j_3 j_4}^{\mathbf{0}; \mathbf{q}, \mathbf{q}'} C_{\mathbf{q}'}^{j_3 j_4} \simeq L \sum_{\mathbf{g}} \Delta_{\mathbf{g}} \chi_{j_1 j_2}^{\mathbf{q}*}(\mathbf{g})$ ]. The two approaches lead to the same superfluid phase, correlation  $C_{\mathbf{q}'}^{j_3 j_4}$ , as well as  $\Delta(\mathbf{r})$  (which is determined by  $C_{\mathbf{q}'}^{j_3 j_4}$ ).

### Effects of different stackings and twist axes

We have focused on the twists starting from  $AA$  stacking with the twist axis at one sublattice site. Like the magic behaviors in TBG [2–5], here the twist axis or stacking position do not affect the appearance of magic flat bands at small twist angles, as shown in Figs. S5a and S5b. When  $\theta$  is small, the Moiré bands for different stackings and twist axes are almost identical. For  $AB$  stacking with twist axis at one coinciding site (where  $A$  site of  $V_\uparrow$  coincides with  $B$  site of  $V_\downarrow$ ), the two valence (conduction) flat bands become degenerate at  $K$  and  $K'$  points and a tiny gap develops between the valence and conduction flat bands. We find that the Moiré bands for  $AB$  ( $AA$ ) stacking with twist axis at one hexagon center is the same as that for  $AA$  ( $AB$ ) stacking with twist axis at one coinciding site. For different stackings and twist axes, the superfluid orders and the phase diagrams are similar, where the pairing order is staggered and distributed mainly around the  $AA$  region (see Fig. S5c).

### Difference with twisted bilayer graphene

In this section, we reemphasize some of the differences between our system and the TBG system.

(1) The two twisted lattice potentials are state dependent, and one potential does not affect atoms trapped by the other. This is different from the electrons in TBG, where electrons in one layer can feel the potential of atoms in the other layer.

(2) Our system is physically a single-layer system and we twist the lattice for atomic (pseudo-)spin states (i.e., atomic internal energy levels). The  $z$ -direction is tightly confined by an additional state-independent potential using the so-called magic-wavelength lasers. Therefore, the two spin states have identical Wannier orbital along the  $z$  direction. The inter-spin tunnelings, realized by additional lasers, are different from the inter-layer tunnelings between  $p_z$  orbitals [2, 3] in TBG where a large inter-layer distance exist. The existence of magic behaviors in our system is not a straightforward derivative of TBG.

(3) The optical lattice potential here takes a cosine form which is much simpler comparing to the atomic potential in graphene. Therefore the bare bands and inter-spin couplings can be obtained accurately by directly solving for the Bloch states  $\phi_{s|\mathbf{k}_s}$  in our system. While for the TBG, real-space tight-binding approximation based on Slater-Koster parameters is usually adopted [2, 3].

- (4) Long-range tunnelings are more significant in our system because the optical lattices considered here are relatively shallow. A shallow lattice not only improves the atomic lifetime (through reducing the atomic decay rate), but also increases the bare Dirac velocity  $v_D$  (a larger  $v_D$  leads to larger gaps and better isolation of the flat bands).
- (5) The interactions are dominated by the  $s$ -wave scattering between atoms in different spin states that are coupled and relatively twisted. In TBG, the electronic interactions are more complex and include both Coulomb repulsive interaction and/or phonon-mediated attractive interactions, which mainly involve electrons in the same layer with no relative twist [11–16]. The unique interaction in our system can lead to interesting Larkin-Ovchinnikov superfluid orders that do not exist in TBG.
- (6) Finally, the advantage of cold atom system is that the parameters (e.g., inter-spin tunnelings, lattice depth, lattice constant, interactions, etc.) are highly tunable. This not only leads to magic behaviors in a wide range of parameter space, but also opens various possibilities for exploring novel twistrionics in cold atom systems.

---

\* xiwang.luo@utdallas.edu

† chuanwei.zhang@utdallas.edu

- [1] T. Li, L. Duca, M. Reitter, F. Grusdt, E. Demler, M. Endres, M. Schleier-Smith, I. Bloch, and U. Schneider, Bloch state tomography using Wilson lines, *Science* **352**, 1094 (2016).
- [2] J. M. B. Lopes dos Santos, N. M. R. Peres, and A. H. Castro Neto, Graphene Bilayer with a Twist: Electronic Structure, *Phys. Rev. Lett.* **99**, 256802 (2007).
- [3] S. Shallcross, S. Sharma, E. Kandelaki, and O. A. Pankratov, Electronic structure of turbostratic graphene, *Phys. Rev. B* **81**, 165105 (2010).
- [4] R. Bistritzer, A. H. MacDonald, Moiré bands in twisted double-layer graphene, *Proc. Natl. Acad. Sci. U.S.A.* **108**, 12233 (2011).
- [5] J. M. B. Lopes dos Santos, N. M. R. Peres, and A. H. Castro Neto, Continuum model of the twisted graphene bilayer, *Phys. Rev. B* **86**, 155449 (2012).
- [6] A. González-Tudela, and J. I. Cirac, Cold atoms in twisted-bilayer optical potentials, *Phys. Rev. A* **100**, 053604 (2019).
- [7] M. Gong, G. Chen, S. Jia, and C. Zhang, Searching for Majorana Fermions in 2D Spin-Orbit Coupled Fermi Superfluids at Finite Temperature, *Phys. Rev. Lett.* **109**, 105302 (2012).
- [8] Y. Xu and C. Zhang, Berezinskii-Kosterlitz-Thouless Phase Transition in 2D Spin-Orbit-Coupled Fulde-Ferrell Superfluids, *Phys. Rev. Lett.* **114**, 110401 (2015).
- [9] X.-J. Liu, K. T. Law, and T. K. Ng, Realization of 2D Spin-Orbit Interaction and Exotic Topological Orders in Cold Atoms, *Phys. Rev. Lett.* **112**, 086401 (2014).
- [10] A. Julku, L. Liang, and P. Törmä, Superfluid weight and Berezinskii-Kosterlitz-Thouless temperature of spin-imbalanced and spin-orbit-coupled Fulde-Ferrell phases in lattice systems, *New J. Phys.* **20**, 085004 (2018).
- [11] T. J. Peltonen, R. Ojajärvi, and T. T. Heikkilä, Mean-field theory for superconductivity in twisted bilayer graphene, *Phys. Rev. B* **98**, 220504 (2018).
- [12] B. Lian, Z. Wang, and B. A. Bernevig, Twisted Bilayer Graphene: A Phonon-Driven Superconductor, *Phys. Rev. Lett.* **122**, 257002 (2018).
- [13] F. Wu, A. H. MacDonald, and I. Martin, Theory of Phonon-Mediated Superconductivity in Twisted Bilayer Graphene, *Phys. Rev. Lett.* **121**, 257001 (2018).
- [14] H. Isobe, N. F. Q. Yuan, and L. Fu, Unconventional Superconductivity and Density Waves in Twisted Bilayer Graphene, *Phys. Rev. X* **8**, 041041 (2018).
- [15] C.-C. Liu, L.-D. Zhang, W.-Q. Chen, and F. Yang, Chiral Spin Density Wave and  $d + id$  Superconductivity in the Magic-Angle-Twisted Bilayer Graphene, *Phys. Rev. Lett.* **121**, 217001 (2018).
- [16] J. González, and T. Stauber, Kohn-Luttinger Superconductivity in Twisted Bilayer Graphene, *Phys. Rev. Lett.* **122**, 026801 (2019).